

Phase Stability and Raman/IR Signatures of Ni-Doped MoS₂ from Density-Functional Theory Studies

Enrique Guerrero, Rijan Karkee, and David A. Strubbe*

Department of Physics, University of California, Merced, Merced, CA 95343

E-mail: dstrubbe@ucmerced.edu

Abstract

Ni-doped MoS₂ is a layered material with useful tribological, optoelectronic, and catalytic properties. Experiment and theory on doped MoS₂ has focused mostly on monolayers or finite particles: theoretical studies of bulk Ni-doped MoS₂ are lacking and the mechanisms by which Ni alters bulk properties are largely unsettled. We use density functional theory calculations to determine the structure, mechanical properties, electronic properties, and formation energies of bulk Ni-doped 2H-MoS₂ as a function of doping concentration. We find four meta-stable structures: Mo or S substitution, and tetrahedral (t-) or octahedral (o-) intercalation. We compute phase diagrams as a function of chemical potential to guide experimental synthesis. A convex hull analysis shows that t-intercalation (favored over o-intercalation) is quite stable against phase segregation and in comparison with other compounds containing Ni, Mo, and S; the doping formation energy is around 0.1 meV/atom. Intercalation forms strong inter-layer covalent bonds and does not increase the *c*-parameter. Ni-doping creates new states in the electronic density of states in MoS₂ and shifts the Fermi level, which are of interest for tuning the electronic and optical properties. We calculate the infrared

and Raman spectra and find new peaks and shifts in existing peaks that are unique to each dopant site, and therefore may be used to identify the site experimentally, which has been a challenge to do conclusively.

March 2, 2021

Transition metal dichalcogenides (TMDCs) are lamellar materials with strong covalent intralayer bonds and weak Van der Waals interlayer bonds. MoS₂ is a semiconducting TMDC with interesting optical,^{1,2} electronic,¹ spintronic,^{3,4} lubrication,⁵ and catalysis⁶⁻⁸ properties, which are often controlled using dopants. Doping MoS₂, especially with Ni, can increase catalytic activity and reduce friction.^{9,10} However, the mechanisms for these doping effects, and even the basic question of the sites occupied by Ni atoms, remain unclear. This work focuses on exploring Ni-doping in bulk 2H-MoS₂ and the effects on materials properties as computed by density functional theory (DFT).

Much previous work about MoS₂, especially doping, has been motivated by catalysis. MoS₂ has properties that are desirable in photo-, electro-, and thermocatalysis.⁶ Though MoS₂ has poor intrinsic catalytic activity, it can be enhanced by dopants¹¹ to create defects (especially at edge sites¹²⁻¹⁵) as active sites. Co- and Ni-doping have been studied theoretically^{12,16} and experimentally^{8,14,17} showing enhancement of the hydrogen evolution reaction. Intercalation by Na, Co, Ni, and Ca has also been shown to increase catalytic activity in 1T-MoS₂.¹⁸

More recently, monolayer MoS₂ has shown promise for optoelectronic applications such as photovoltaics¹⁹ or LEDs.²⁰ Large exciton binding energies and long lifetimes of excitons in MoS₂ mean that the high absorption rate can be used to generate useful excitons at room temperature.^{19,21-23} Dopants can alter the Fermi energy by donating or accepting electrons and can tune these optoelectronic properties.¹ Monolayer and bulk 3R MoS₂ lack inversion symmetry, unlike the bulk 2H phase, giving rise to spin-orbit effects which can further be exploited for spintronic and valleytronic applications.^{3,23} Transition metal doping by Mn, Fe, Co, and Zn has been used to induce magnetism which could be used for spintronics.^{11,24}

Bulk MoS₂ also has useful properties for the older application of lubrication: superior resistance to wear (the gradual loss of material caused by sliding¹⁰) and a low coefficient of friction (high lubricity) due to the ease of shearing along the basal plane.²⁵ As a solid lubricant, MoS₂ holds some advantage over liquid lubricants—notably it lubricates at temperatures and pressures low enough even for space applications.⁵ Tribological properties can be enhanced via doping.¹¹ Re (in MoS₂ fullerene-like nanoparticles²⁶) and Ta⁹ have been observed to increase lubricity, and Cr and Ti have been found to strengthen the resistance to humidity while retaining MoS₂'s high lubricity.²⁷ Ni is an exceptional dopant for increased wear protection, decreased coefficient of friction, and long-term stability.⁹ Despite how long studied these materials are, correlation of macroscopic tribological properties and microscopic atomic structure has remained elusive, especially for 2D materials.^{5,28,29}

Previous studies suggest that Ni substitutes Mo at edge sites in small flakes,^{12–15} but there has been little investigation of Ni-doping in bulk. Some possibilities are suggested by studies of other dopants. Co³⁰ (chemically similar to Ni) and Ta³¹ are thought to increase catalytic activity by insertion into S vacancies near the usually inert basal plane. In bulk, other ions^{32–34} can intercalate between the layers or even form ordered alloys.³⁵ A phase change from 2H to 1T with Li intercalation has been found via Raman spectra indicating a symmetry change from D_{6h} to D_{3d} and increased interlayer spacing.³² Ni-doping, presumably through surface energies, can control MoS₂ crystal size and growth rates.^{8,17} A study of Ni-doped MoS₂ nanostructures found signs of Ni substitution for Mo and a change to the 3R phase; shifts in diffraction peaks indicated contraction of the MoS₂ cell.⁸

Vibrational spectroscopy has been a main tool for the characterization of 2D materials and their defects. *n*-type doping of MoS₂ is correlated with redshifts of the A_{1g} Raman-active peak and *p*-type with blueshifts while the E_{2g}^1 Raman frequency remains unchanged. This behavior is found in field-effect doping as well.³⁶ With other transition metals, Nb-doping was found to cause an A_{1g} redshift³⁷ while Au caused a blueshift.³⁸ An A_{1g} redshift around 1 cm⁻¹ for Ni-doped MoS₂ nanostructures was attributed to changes in number of layers.⁸

A new 280 cm^{-1} peak was found in Ni-doped MoS_2 that was not related to either pure MoS_2 or nickel sulfides,¹⁷ but its origins have not been further characterized. Vibrational properties are also important for tribology as energy dissipation via vibrational states^{28,39} and electron-phonon coupling²⁹ (EPC) are thought to play a crucial role in increasing friction in 2D materials. We have not found previous vibrational spectra computations of doped bulk 2H- MoS_2 and experimental reports have rarely had sufficient resolution to identify dopant-related peaks. There is a clear need for more detailed Raman and IR studies since vibrational spectroscopy can be a powerful tool for characterizing defects.

In this paper, we use first principles DFT calculations to systematically survey different structures and concentrations of bulk Ni-doped MoS_2 to definitively resolve the structure of this material. We determine phase stability to guide synthesis and show unusual stability of intercalated structures. We compute Raman and IR spectra to aid in experimental identification of defect structures (which may not be lowest energetically due to non-equilibrium growth), and study elastic and vibrational properties to understand how Ni improves performance in lubrication. By studying elasticity, bonding, and vibrations, we elucidate how Ni decreases friction and increases resistance to wear.

1 Results and Discussion

We consider a set of possible dopant sites shown in Fig. 1: Mo substitution, S substitution, octahedral (o-) intercalation, and tetrahedral (t-) intercalation, as studied for Nb-doped MoS_2 .⁴⁹ Other possible sites included the bridge site above an Mo-S bond and in between two layers, and the hollow-site interstitial directly between three S atoms on the S plane. These were ruled out as possibilities because they were found to be unstable under relaxations—they both relaxed to o-intercalation.

We consider doping of the most common MoS_2 structure: 2H, belonging to the D_{6h} point group with 6 atoms per unit cell, which is very close in energy to the 3R bulk phase.⁵⁰

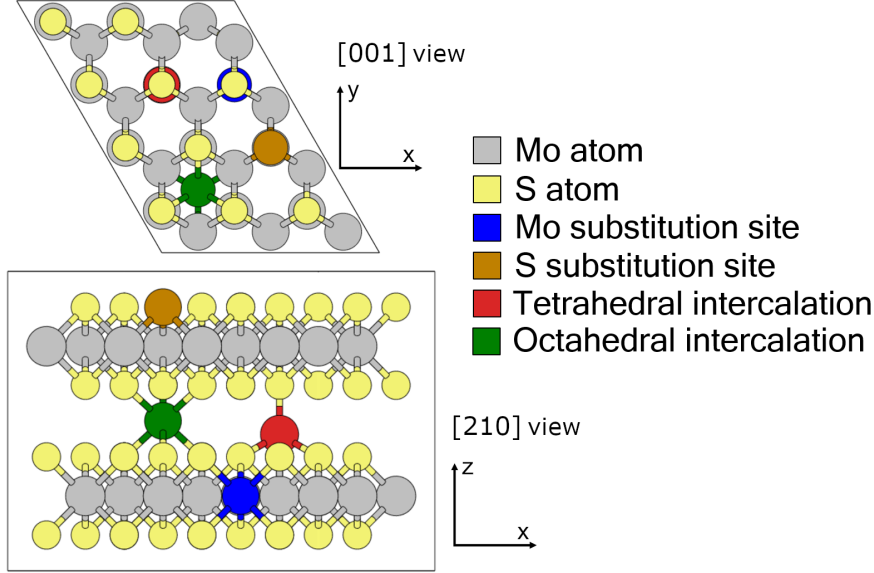


Figure 1: Possible sites for Ni dopants in 2H-MoS₂: Mo or S substitution, or intercalation at tetrahedral (t) and octahedral (o) interlayer sites. Other highly symmetric sites (bridge and intralayer interstitials) were found to be unstable.

Introducing Ni lowers symmetry: Mo substitution, S substitution, o-, and t-intercalation structures belong to the D_{3h} , C_{3v} , D_{3d} , and C_{3v} point groups respectively. We considered doped structures of increasing MoS₂ supercell size in-plane from 1×1 to 4×4 , each with 1 Ni atom per cell, with Ni concentrations of 16.7 at%, 4.2 at%, 1.9 at%, and 1.0 at%. Decreasing Ni concentration allows us to extrapolate quantities to the low-doping limit.

Van der Waals interactions are important between MoS₂ layers, but they are a challenge for DFT calculations. Since such interactions are almost absent in PBE, we considered PBE with and without Grimme-D2 (GD2)⁵¹ Van der Waals corrections. We found Grimme-D3⁴⁸ to give very similar structures to GD2. However, GD2 and related approaches are particularly poor for metals.⁵² This is not an issue for MoS₂, but it is problematic for computing formation energies with reference to pure Ni and Mo. By contrast, LDA is quite accurate for metals, and also successful for Van der Waals-bonded quasi-2D systems: empirically, it is seen that LDA's overestimation of interatomic interactions balances the lack of explicit non-local Van der Waals interactions.⁵³ Therefore we focus on LDA for formation energies such as in Table 2. We also find that LDA provides better agreement with experimental vibrational

Table 1: Comparison of Lattice Parameters, Vibrational Frequencies at $q = 0$, and Elastic Parameters

	This Work			Literature		
	LDA	PBE	PBE + GD2	Exp't	LDA	PBE + vdW [†]
a (Å)	3.12	3.18	3.19	3.16 ⁴⁰	3.13 ⁴¹	3.16 ⁴²
c/a	3.87	4.64	3.89	3.89 ⁴⁰	3.89 ⁴¹	3.89 ⁴²
E_{2g}^1 (cm ⁻¹)	389	373	371	383 ⁴³	388 ⁴¹	372 ⁴⁴
A_{1g} (cm ⁻¹)	413	402	403	409 ⁴³	412 ⁴¹	397 ⁴⁴
E_{1u} (cm ⁻¹)	390	373	372	384 ⁴³	391 ⁴¹	372 ⁴⁴
A_{2u} (cm ⁻¹)	471	458	457	470 ⁴³	469 ⁴¹	454 ⁴⁴
C_{11} (GPa)	242	181	212	238 ⁴⁵	240 ⁴⁶	223 ⁴²
C_{33} (GPa)	53	1.70*	51	52 ⁴⁵	53 ⁴⁶	49 ⁴²
C_{55} (GPa)	20	0.76*	15	19 ⁴⁵	32 ⁴⁶	15 ⁴²

*PBE without Van der Waals underestimates the elasticity in the z -direction.

[†]Ref.⁴⁴ seems to use Tkatchenko-Scheffler⁴⁷ dispersion corrections while Ref.⁴² uses Grimme-D3.⁴⁸

frequencies than PBE or PBE+GD2 (Table 1).

With these considerations, we have chosen to use LDA calculations for energies in the phase diagrams, convex hull, and vibrational calculations. As shown by Peelaers and Van de Walle, adding dispersion corrections to PBE can give reasonable structures and elastic properties;^{54,55} we confirm this in Table 1. PBE+GD2 was thus used for structural parameters, elastic parameters, and electronic densities. PBE with no correction was found to be quantitatively worse than LDA and is not used except as a point of comparison: the energy landscape is very flat with respect to changes in layer separation, leading to large errors in the lattice parameter c and the C_{33} and C_{55} parameters.

We calculated formation energy for pristine and doped MoS₂, as well as other crystals containing Mo, S, and/or Ni. We used the Materials Project⁵⁶ to find materials with relatively stable computed energies (less than 0.1 eV/atom above hull): Ni₂Mo, Ni₃Mo, Ni₄Mo, NiS₂, Ni₃S₄, NiS, Ni₉S₈, Ni₃S₂, MoS₂, and Mo₃S₄, and the Chevrel phase NiMo₃S₄. Details on the calculation parameters for the structures used can be found in Table S1. NiMo₃S₄⁵⁷ appears to be the only known stoichiometric crystal that contains all three species. It could be a competing material during the synthesis of Ni-doped MoS₂, and has been studied for

catalysis of the hydrogen evolution reaction.⁷

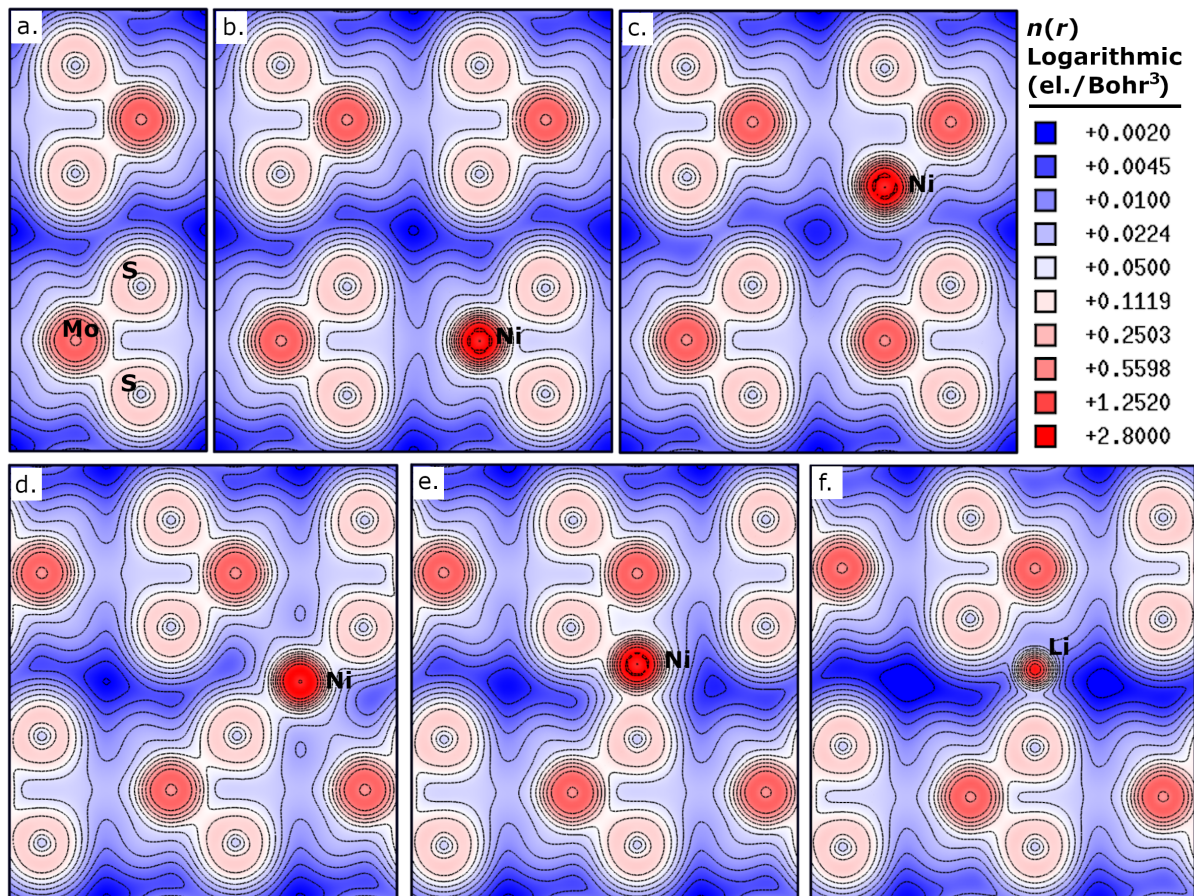


Figure 2: Cross sections of the electron densities of a) pristine MoS_2 , b) Ni substituting Mo, c) Ni substituting S, d) Ni o-intercalation, e) Ni t-intercalation, and f) Li t-intercalation within 2×2 supercells. The data is displayed in a logarithmic color scale in the xz -plane which includes Mo-S and Ni bonds. In intercalated structures, the electron density has strongly increased in the interatomic region between layers. This suggests formation of covalent bonds for intercalated Ni, unlike in the well-known case of Li.⁵⁸ Densities were plotted using XCrysDen.⁵⁹

The electron density can be a useful tool to study bonding. The pristine unit cell and doped 2×2 supercell electron densities are shown in Fig. 2. The maximum electron density in the Ni-S or Ni-Mo bonding regions is similar to that of the pristine Mo-S bonds, signifying the Ni bonds are strong and covalent in all cases. The maxima are slightly less than for Mo-S bonds in each case, except they are higher for the Ni-S interlayer bonds of t-intercalation. The surprising result that Ni can readily substitute S with the bonding network intact indicates

that Ni, like Co,³⁰ could potentially be used to fill S vacancies in a stable structure. Results from formation energies with respect to vacancies, however, show that filling an S vacancy with Ni requires energy while filling a Mo vacancy with Ni releases energy (Table S6).

The o- and t-intercalated structures show clear layer-to-layer bonds with the Ni atom as a bridge. Li is a known MoS₂ intercalant that widens the separation between layers⁵⁸ and is stripped of its outer electron, leaving a closed-shell ion that does not form covalent bonds, as shown in Fig. 2f. Comparing the Li case to Ni shows a stark contrast in the electron density, indicating that Ni forms strong covalent interlayer bonds as opposed to Van der Waals or ionic interactions for Li. The interlayer density is unchanged from the pristine in the Mo-substituted case but has increased significantly in the case of S substitution, indicating increased interlayer interactions.

We find a small reduction in the *c*-parameter for Mo substitution, as well as for S substitution and o-intercalation, especially at high concentration. This is consistent with Mosconi *et al.*'s report that Ni-doping results in reduction of the *c*-parameter, attributed to Mo substitution and Ni's smaller covalent radius.⁸ The basal lattice parameter *a/b* is essentially unchanged, however, regardless of concentration. 3×3 and 4×4 supercells of Mo-substituted and o-intercalation structures show a pseudo-Jahn-Teller symmetry-breaking in their Ni-S bond lengths. When Ni substitutes Mo, four Ni-S bonds are 2.2 Å long (2 bonds to each of the S planes), an additional bond is slightly longer by 0.2 Å and the final S atom has been pushed away significantly to a distance of 3.3 Å. A similar symmetry-breaking has been calculated for Mo substitution on the basal plane.¹⁶ A fully symmetric o-intercalation structure is possible, unlike the t-intercalation which automatically breaks symmetry between layers. Despite this, o-intercalation breaks symmetry: Ni-S bonding distances in the closer layer are 0.2 Å shorter than those in the further layer. A full concentration dependent set of atomic distances and cell parameters can be found in Table S2.

Since the different doped structures have different stoichiometries, we compare their thermodynamic favorability using not only formation energies but also the chemical potentials

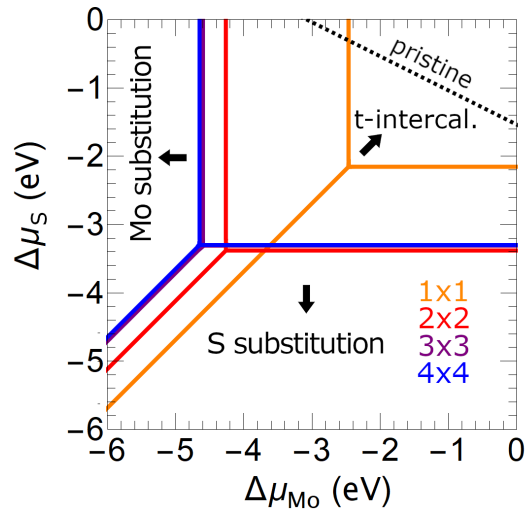


Figure 3: Thermodynamically favored doped structures at different chemical potentials relative to bulk phases, as calculated by LDA. The equilibrium lines change depending on the concentration, but do not change much between LDA, PBE, and PBE+GD2. The dashed line indicates the boundary above which MoS_2 is stable. Phase diagrams for PBE and PBE+GD2 can be found in Fig. S1.

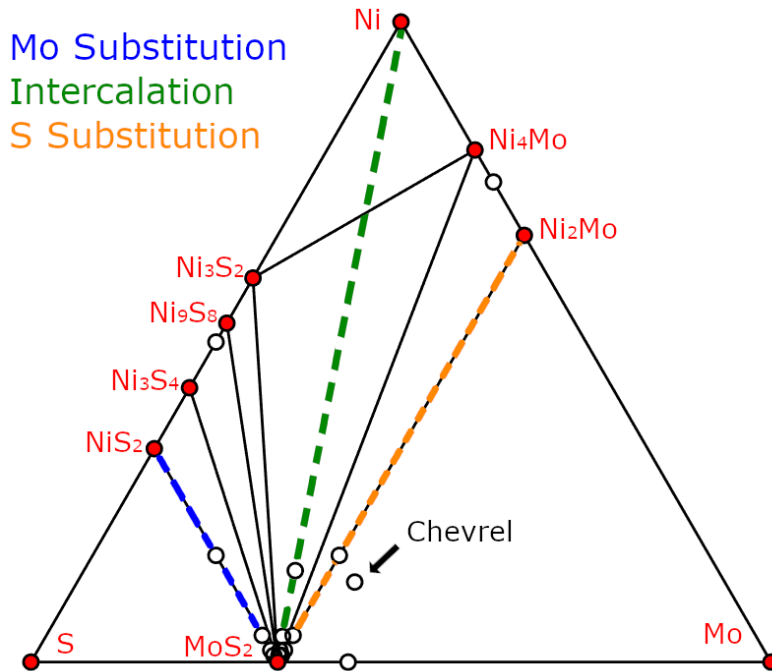


Figure 4: Phase diagram for materials containing Ni, Mo, and S, based on LDA energies. Materials' position along the plane edges indicate their stoichiometry. Materials on the convex hull are shown in red. Structures with energies above hull are represented as open circles; all the doped structures fall within this category and are mostly clustered around the MoS_2 point. The t-intercalation is above but very close to the convex hull.

Table 2: Energies per Atom Above Hull in eV, According to LDA, for Computed Solids Containing Mo, S, and/or Ni.

Mo	0	Ni ₃ Mo	0.024	NiS	0.018	MoS ₂	0
Ni	0	Ni ₄ Mo	0	Ni ₃ S ₄	0	Mo ₃ S ₄	0.065
S	0	NiS ₂	0	Ni ₉ S ₈	0		
Ni ₂ Mo	0	NiMo ₃ S ₄	0.050	Ni ₃ S ₂	0		
		Mo subst.	S subst.	t-intercal.		o-intercal.	
1×1		0.149	0.173	0.025		0.116	
2×2		0.107	0.090	0.002		0.044	
3×3		0.054	0.039	0.001		0.021	
4×4		0.031	0.022	0.001		0.012	

of the elements with respect to their bulk phases. The favored structures as a function of chemical potentials are shown in Fig. 3. We focus on the region with $\Delta\mu_S \leq 0$ and $\Delta\mu_{Mo} \leq 0$, where the bulk Mo and S would not be formed, as in stability triangle analysis.⁶⁰ With different supercell sizes, and thus concentrations, the favorable chemical potential regions shift slightly. Except for the very highly-doped 1×1 structure, the triple point rests around $\Delta\mu_{Mo} = -4.0$ eV and $\Delta\mu_S = -3.7$ eV. These values can be used to select the relative concentrations of reactants used in the synthesis process to achieve a particular target structure. The proximity of the 3×3 and 4×4 lines show that the 3×3 supercell is converged to the low-doping limit. O-intercalation structures do not appear on this plot because they have the same stoichiometry as t-intercalation, but always have a larger formation energy by about 0.07 eV per Ni atom. For comparison, calculations indicate o-intercalation is preferred over t-intercalation for Nb,⁴⁹ Li,⁵⁸ and Mo.⁶¹ The stability line⁶⁰ for pristine MoS₂ is also shown in Fig. 3, below which any kind of MoS₂ structure is not expected. Since only the t-intercalation region (for supercells greater than 1×1) exists above this line, we conclude that equilibrium growth will yield t-intercalation, and the substituted sites can only be reached out of equilibrium. Phase diagrams for PBE and PBE+GD2 are shown in Fig. S1 and show a similar trend to LDA with respect to increasing supercell sizes. Formation energies *vs.* bulk Mo and S (Table S4) are -0.6 to -1.0 eV, but to judge favorability of doping, we must compare to MoS₂. Previous studies⁶² have focused on the end-points of this pristine stability

line: where $\Delta\mu_S = 0$ (“S-rich”) or $\Delta\mu_{\text{Mo}} = 0$ (“Mo-rich”). We consider in both cases that $\Delta\mu_{\text{Ni}} = 0$, *i.e.* “Ni-rich” as well. We find that t-intercalation is the favored structure for both ends at all supercell sizes, except for 1×1 where S-rich conditions favor Mo-substitution. The positive formation energies *vs.* MoS_2 (0.01-0.4 eV) in Table S5 show that doping is unfavorable generally, though t-intercalation is essentially stable with an extremely small formation energy of ~ 0.1 meV/atom.

The convex hull is used to identify structures that are stable against phase segregation.^{63,64} Our calculation (Fig. 4) shows that neither the Chevrel nor the doped compounds are the most stable structures at their concentrations. Therefore, these structures will phase-segregate into nickel sulfides, Ni-Mo alloys, and pure elements given enough time and temperature. Table 2, however, shows that the low-concentration doped structures have small energies above hull. The t-intercalation energies above hull, in fact, are below $k_B T$ at room temperature for all concentrations, and have magnitude within the margin of error for DFT energies. Therefore we may regard these structures as stable: synthesizable and unlikely to phase-segregate. Despite being observed at the edges of small flakes,¹⁴ Mo substitution has high energies above hull which are generally higher than for S substitution. The Chevrel phase (NiMo_3S_4) has an energy above hull on the order of the 3×3 Mo- and S-substituted phases—since this phase is known to be experimentally synthesizable,⁵⁷ the results suggest the doped phases will also be accessible. Consideration of 1D convex hull plots along the colored lines of Fig. 4 shows very small energy differences above hull for t-intercalation *vs.* MoS_2 and bulk Ni, but much larger differences for Mo substitution *vs.* MoS_2 and NiS_2 , or S substitution *vs.* MoS_2 and MoNi_2 (Fig. S3). Several Ni_xS_y phases are seen to be stable, consistent with observation of their forming during synthesis by Kondekar *et al.*¹⁷ Phase diagrams for PBE and PBE+GD2 and energies above hull are given in Fig. S2 and Table S3.

We found the elastic parameters, important for tribology as the material is under stress, are altered by Ni-doping as shown in Table 3. The in-plane C_{11} parameter is notably weak-

Table 3: Elastic Parameters for Ni-Doped Structures at Different Supercell Sizes.*

(GPa)		undoped	Mo subst.	S subst.	t-intercal.	o-intercal.
C_{11}	1×1	211.8	159.2	168.9	201.4	208.2
	2×2	"	177.2	204.8	211.5	210.6
	3×3	"	196.5	207.7	211.1	208.7
	4×4	"	190.8	210.0	212.0	210.2
C_{33}	1×1	51.3	50.0	91.7	99.4	94.1
	2×2	"	51.3	57.7	76.1	72.9
	3×3	"	49.0	55.8	63.4	63.3
	4×4	"	50.0	54.3	57.9	58.7
C_{55}	1×1	15.1	7.5	24.3	24.0	25.3
	2×2	"	13.1	10.9	19.1	20.6
	3×3	"	13.8	14.0	16.7	12.4
	4×4	"	14.2	14.6	15.9	13.2

*1×1 through 4×4 supercells correspond to Ni concentrations of 17 at%, 4 at%, 2 at%, and 1 at% respectively. Most structures did not change appreciably in C_{11} besides the 20-30 GPa drop for Mo substitution. C_{33} values were appreciably raised by 20 GPa in intercalated cases. C_{55} did not show large changes, giving evidence against the idea that Ni-doping lowers the frictional coefficient by lowering the shear stiffness.

ened in the case of Mo substitution. This may be related to the lower charge density between Ni and S as seen in Fig. 2b. At lower Ni concentrations, the reduced number of bonds leads to a lower C_{11} . S substitution also weakened C_{11} slightly, but the intercalated cases saw little change at any supercell sizes beyond 1×1. Out-of-plane C_{33} stiffness increased in the case of intercalated and S-substituted structures due to interlayer bonding with intercalated Ni, and increased interlayer interactions for S substitution. The increased out-of-plane stiffness will contribute to the increased resistance to wear (layers flaking off), as seen in experiments.^{9,10}

Since Ni-doping is known to reduce the coefficient of friction of MoS₂, we might expect C_{55} would be lowered, reducing the shear stiffness. However, there is not much difference between doped and undoped C_{55} values at low concentrations. Further, at high concentrations (5-15 at%) C_{55} of intercalated structures is significantly higher than the pristine case (except for Mo substitution, where it is halved). This indicates that a reduction in shear stiffness is not the explanation for the observed reduction in frictional coefficient due to Ni-doping.

To aid in experimentally identifying Ni-doped MoS₂, we have computed the Raman and

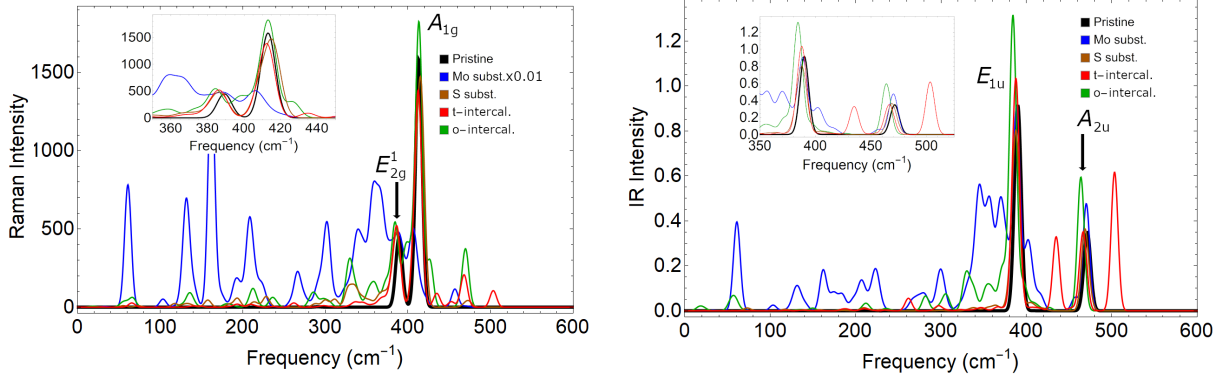


Figure 5: Raman and IR spectra, in $\text{Å}^4/\text{amu}$ per MoS_2 unit and $(\text{D}/\text{A})^2/\text{amu}$ per MoS_2 unit respectively, for 3×3 doped structures. A Gaussian broadening of 4 cm^{-1} is used. Mo-substituted Raman intensities are large, so they are scaled by a factor of 0.01. Low frequency modes ($< 100\text{ cm}^{-1}$) correspond to layer breathing and shearing modes. Insets more closely show the pristine Raman-active A_{1g} and E_{2g}^1 modes and IR active E_{1u} and A_{2u} modes. The strong IR and Raman peaks of the pristine MoS_2 remain with doping but new peaks appear at different frequencies which can be used for experimental identification of the doping site.

IR intensities for MoS_2 with the different doped sites. Previous experimental work^{8,37,65} on doped MoS_2 has focused on shifts in the A_{1g} and E_{2g}^1 Raman peaks relative to the pristine positions,⁶⁶ but has not investigated the formation of new peaks due to the presence of a new atom of a different mass, or symmetry-breaking due to the dopant, as seen in other doped 2D materials;^{67,68} one exception is the study of Li-intercalated MoS_2 by Sekine *et al.*⁶⁹ Raman and IR spectra are compared in Fig. 5 and key distinguishing features are listed in Table 4. Mode characters are detailed in Tables S7-10. We have computed the spectra for 1×1 , 2×2 , and 3×3 supercells to see the concentration-dependence of the strong Raman and IR active peaks and find that 3×3 is converging to a low-doping limit (Figs. S5 and S6), though significant Raman intensity variations with concentration remain for Mo substitution and o-intercalation.

As in previous studies,^{17,37,70} the doped spectra show peaks corresponding to the pristine ones, with changes in frequency. Shifts in the pristine Raman/IR peaks can be caused by a number of factors: the mass difference of Ni compared to substituted Mo or S, an alteration of bond strengths by n - or p -type doping, or induced strain.⁷¹ Ni has two more electrons than Mo and results in n -type doping (as discussed below), which would generally

Table 4: Changes to the Pristine Vibrational Spectra for Doped 3×3 Structures.

Frequency (cm ⁻¹)		Mo subst.	S subst.	t-intercal.	o-intercal.
Raman	New peak	61, 131, 132, 162, 266, 301, 364	327, 333, 337	366, 372, 435, 452, 503	212, 235, 330, 361, 427
	Activation	209, 457	473	336, 465, 468	67, 135, 287, 287, 470
	E_{2g}^1 shift	-3.2	-3.2	-3.1	-5.4
	A_{1g} shift	-7.1	+2.0	-0.2	-0.5
IR	New peak	61, 131, 132, 162, 301, 345, 356, 370	-	262, 435, 503	330
	Activation	209, 224, 388, 389, 470	473	465, 468	54, 59, 282, 282
	E_{1u} shift	-0.6	-0.8	-1.9	-6.1
	A_{2u} shift	-14.5	-3.0	-6.2	-7.5

 Table 5: Calculated $q = 0$ Low-Frequency Vibrational Modes in Pristine and Doped MoS₂.

(cm ⁻¹)	undoped	Mo subst.	S subst.	t-intercal.	o-intercal.
Shearing-like mode frequency (pristine E_{2g}^2)					
1×1	35	38, 43	88, 89	57, 57	48, 49
2×2	"	26, 30	24, 27	42, 43	41, 41
3×3	"	32, 34	22, 25	30, 30	17, 22
Layer breathing-like mode frequency (pristine B_{2g}^2)					
1×1	56	88	132	127	108
2×2	"	63	58	78	71
3×3	"	59	55	66	67

be expected to result in a redshift of the A_{1g} peak.⁶⁶ In Li-intercalated MoS₂, Sekine *et al.*⁶⁹ experimentally found redshifts of the E_{2g}^1 and A_{1g} Raman frequencies due to changes in the c -axis interactions. Table 4 shows that in Ni-doped MoS₂ A_{1g} has small redshifts for intercalation, like Li-intercalated MoS₂, but A_{1g} has a blueshift for S substitution. Dopants have generally been found to shift mostly the A_{1g} frequency,⁶⁶ including the measurement of a shift around -1 cm⁻¹ for E_{2g}^1 and $+3$ cm⁻¹ for A_{1g} in Ni-doped MoS₂;¹⁷ however, in our calculation we find Ni induces also strong shifts in the E_{2g}^1 peak and the IR-active peaks. The different behavior observed in the experiment may be due to different (and unclear) Ni concentration and the effects of a limited number of layers, in-plane crystallite size, and/or

strain.¹⁷

Peaks unique to the doped spectra were classified as either “new” or “activations.” New peaks are those that do not have counterparts in the pristine 3×3 q -grid vibrational density of states (VDOS) (Fig. S4) and have mode characters that cannot be easily described by pristine mode eigenvectors: they are mostly related to motions of the Ni atom and its neighbors. Such new peaks were measured in Li-intercalated MoS₂ at 205, 1370, and 1600 cm⁻¹.⁶⁹ Activations are modes that have a counterpart in the pristine case whose IR and/or Raman activity is forbidden by symmetry. Ni-doping breaks symmetries and mixes modes, which can induce IR and/or Raman activity. Raman intensities were particularly large in the case of Mo substitution owing to its metallic character, and so they are scaled down in Fig. 5; we expect this intensity enhancement compared to pristine can serve as a feature to identify this kind of doping. There is Raman and IR activity present in all doped structures at low frequencies (below 350 cm⁻¹), but it is most prominent in Mo-substituted and o-intercalation structures.

The modes of the doped systems show several interesting patterns in comparison to the pristine modes (Fig. 6). Many new modes are breathing modes of Mo and S around Ni (Fig. 6a), or involve Ni-S stretches (Fig. 6b), or feature new combinations of S motions, as in S substitution or Mo substitution. The activation peaks are strongly influenced by symmetry breaking between the two layers. In Mo and S substitution, only one layer has a dopant, strongly breaking symmetry; pristine modes are mixed to give modes localized on only layer (Fig. 6c). In t-intercalation, the layer symmetry is broken because Ni has 3 bonds to one layer and 1 to the other, and so the activations involve Mo/S motion in only one layer. For o-intercalation, a perfectly symmetrical structure is possible, but in fact Ni moves slightly closer to one layer, making only a small symmetry breaking: most activated modes (Fig. 6d) are still on both layers, look identical to pristine, and are shifted typically less than 10 cm⁻¹ from the pristine frequencies. Most of the new peaks also show these same layer localization patterns.

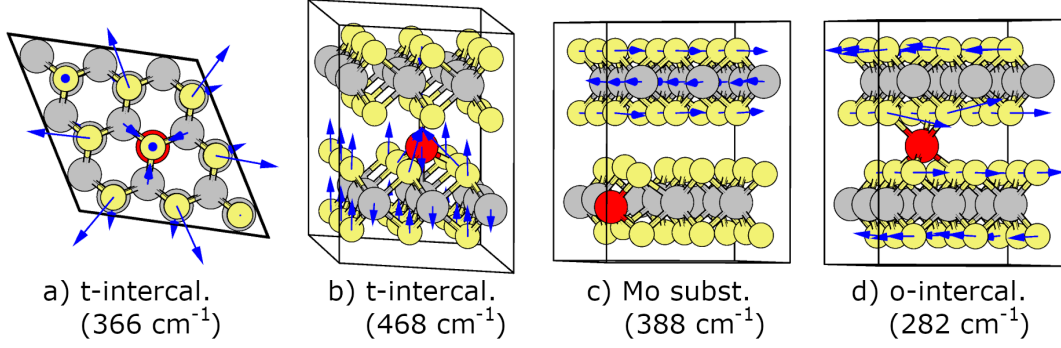


Figure 6: Example vibrational modes of Ni-doped MoS₂, showing four typical patterns: a) a new peak for t-intercalation consisting of an in-plane breathing mode around Ni, in only one layer; b) t-intercalation breaks symmetry between the layers, mixing the A_{2u} and B_{2g}^1 modes with Ni-S stretches; c) Mo substitution breaks symmetry between layers, and mixes E_{2g}^1 and E_{1u} modes, but does not involve Ni; d) o-intercalation only slightly breaks symmetry, and leaves E_{2u} modes almost unaffected.

Kondekar *et al.*¹⁷ find a Raman peak related to Ni-doping at 290 cm⁻¹. This peak seems a sign of Mo-substitution, corresponding to our calculated new peak at 300 cm⁻¹, which is related to S vibration in the doped layer, out-of-phase between the two S planes. This peak appears for both 2×2 and 3×3 supercells and should be detectable given the high Raman intensity. A less likely possibility (due to lower intensity, and unfavorable energetics) is the o-intercalation, which has a peak at 287 cm⁻¹ related to the pristine E_{1g} (low Raman activity) and E_{2u} (Raman-inactive) modes. With higher-resolution Raman spectroscopy, we expect that additional peaks could be discerned and solidify the identification.

A few low-frequency modes are particularly relevant to tribology: the shearing mode (E_{2g}^2 in pristine), relating to frictional sliding, and the layer breathing mode (B_{2g}^2 in pristine), relating to layer dissociation and wear. Our calculated values for the doped structures are listed in Table 5. The increase in the layer breathing frequency in intercalated structures correlates with the stiffening of C_{33} in those structures. Substituted breathing mode frequencies are largely unaffected. The doubly degenerate shearing mode was split in the doped structures, and reduced in frequency for low doping concentration, particularly in S substitution and o-intercalation. At high doping concentrations, both shearing and breathing frequencies are increased.

Raman intensities are related to EPC and have been suggested as a probe of EPC in 2D materials.⁷² In our systems, only Mo substitution shows substantial changes in intensities, whereas other sites stay within 10% of the pristine peak intensity. If the argument by Lin *et al.*⁷² applies, Mo substitution’s large Raman intensity would mean increased EPC and thus increased friction. This means that the observed reduction in friction^{9,10} of Ni-doped MoS₂ is either not attributable to changes in EPC or samples were not dominated by substitution of the Mo site.

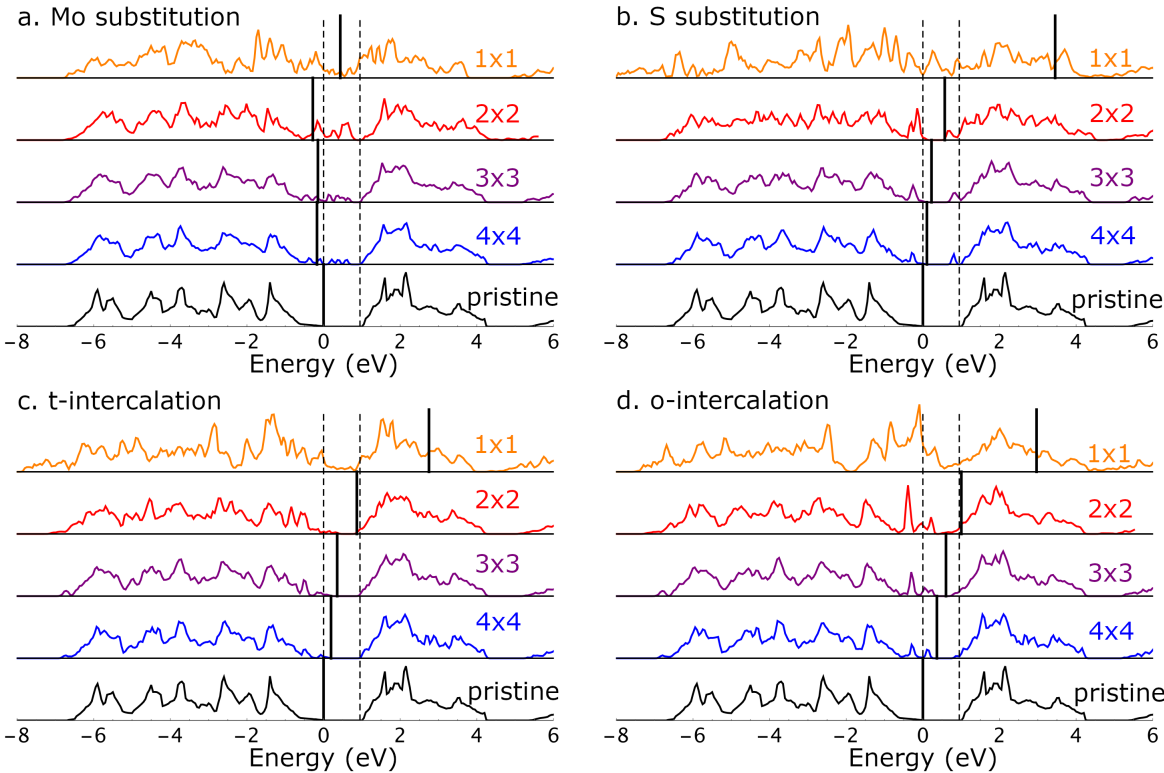


Figure 7: Electronic density of states (DOS) for doped structures (color) and pristine DOS (black). The CBM and VBM of pristine MoS₂ are shown as vertical dashed lines. Doped DOS were aligned with the low-lying Mo 4s state (36 eV below VBM) of the pristine plot. Calculated Fermi energies or VBM are shown as solid-black vertical lines.

To assess *n*-type or *p*-type doping and other changes in electronic structure, we calculate the electronic density of states (DOS), shown in Fig. 7. Low concentrations of S-substituted structures show defect states near the conduction band maximum (CBM) while

o-intercalation creates defect states above the valence band maximum (VBM). All doped structures show some degree of bandgap closing. Mo-substituted structures have metallic character, with the Fermi level situated in the new in-gap states meaning it is slightly p -type. S substitution shows new states near both band edges, while o-intercalation has new states near the valence band and an extended conduction band tail. The t-intercalation shows the least modification from the pristine DOS, with only a slight narrowing of the gap due to new states in the valence band.

The Fermi level for low doping concentration is near the pristine VBM. Alterations are more dramatic at high concentrations where the Fermi level is pushed well within the pristine conduction band in all cases except Mo substitution. This can be understood as n -type doping at high concentration. Naturally occurring MoS₂ is typically n -type due to Re impurities.⁷³ Provided nickel sulfides do not form,¹⁷ high Mo-substitution doping concentrations could create p -doped MoS₂, which has been challenging to achieve.⁷⁰

In general, our calculations indicate an increased conductivity of Ni-doped MoS₂, either through in-gap states, a narrowed bandgap, or n - or p -type electronic doping, depending on the doping site. These results are consistent with enhanced catalytic activity of Ni-doped MoS₂, and early calculations attributing enhancement in Mo-substituted MoS₂ to electron donation from Ni to Mo.⁷⁴

2 Conclusion

Through *ab initio* methods, we have computed the structure, stability, and vibrational spectra of bulk Ni-doped 2H-MoS₂, which has not been previously explored. We found four metastable dopant sites: Mo substitution, S substitution, octahedral intercalation, and tetrahedral intercalation (always favored energetically over octahedral). Ni in the Mo-substituted structure has only five bonds just as in a basal plane surface,¹⁶ and thus is elastically weaker in-plane. The C_{55} shear-stiffness parameter is strengthened by doping, suggesting this is

not the explanation for the reduced friction observed⁹ in Ni-doped MoS₂. Ni-S bonding is comparable to pristine Mo-S bonding, and the fact that Ni-Mo bonds are comparable to Mo-S bonds in S substitution are particularly surprising—this suggests that Ni, like Co,³⁰ can fill existing S vacancies as a way to synthesize S-substituted MoS₂.

We find that all doped structures are above the convex hull, but t-intercalation is very close to it. It therefore can be considered thermodynamically stable, with essentially zero formation energy from Ni and MoS₂, and is not likely to phase-segregate, unlike the other doped structures. The other sites’ energies above hull are lower than that of the known Chevrel phase NiMo₃S₄, suggesting these are synthesizable as well. Phase diagrams show how the chemical potentials of Mo and S can be tuned in synthesis to favor Mo substitution, S substitution, or t-intercalation, though only t-intercalation can co-exist with pristine MoS₂. Intercalated Ni forms strong covalent bonds between layers, unlike intercalated Li. This increases elastic parameters out of plane, and results in little change to the *c*-parameter, contrary to what is sometimes assumed. Strong interlayer bonding poses a possible explanation for the observed resistance to wear.^{9,10}

n-type doping is prominent at high Ni concentration. Mo-substituted structures become metallic due to in-gap states, which leads to a large enhancement of Raman intensities. New peaks in the Raman spectra appear due to vibrations of Ni and its neighbors, while activations and shifts in existing modes are caused by breaking symmetry and altering bond strengths. While generally doping has been found primarily to affect the *A*_{1g} mode, we find shifts of all four IR- and Raman-active peaks. The distinctive effects on the Raman and IR spectra can be used experimentally to identify the doping sites in Ni-doped samples, particularly with high-resolution, tip-enhanced, or resonant Raman spectroscopy. We propose a new paradigm for identification of MoS₂ dopant locations by vibrational spectroscopy, as these structures have remained unclear experimentally.

The structures found in this work are being used to probe macroscopic tribological properties related to wear and friction through parametrization of ReaxFF force fields⁷⁵ for

classical molecular dynamics and calculations of sliding potentials.⁷⁶ We are additionally extending this work to study Ni-doping in 3R bulk and 1H and 1T monolayer polytypes of MoS₂⁷⁷ to determine the impact of the phase on doping effects.

3 Methods

3.1 DFT Calculations

We use plane-wave density functional theory (DFT) and density functional perturbation theory⁷⁸ (DFPT) implemented in the code `QUANTUM ESPRESSO`^{79,80} version 6.4. Calculations were performed using the Perdew-Burke-Ernzerhof⁸¹ (PBE) generalized gradient approximation and Perdew-Wang⁸² local density approximation (LDA) exchange-correlation functionals with optimized norm-conserving Vanderbilt pseudopotentials⁸³ parametrized by Schlipf and Gygi⁸⁴ (for PBE) and by PseudoDojo⁸⁵ (for LDA) obtained from their respective websites.^{84,85} Raman calculations were done only for LDA since PBE is not compatible with Raman intensity calculations in this code.⁸⁶

Relaxations and electronic structure of the primitive, 6-atom MoS₂ cells used a k -point grid of $6 \times 6 \times 4$ with a half-shifted k -grid. Increasing the supercell size to reach lower Ni concentrations allows decreasing k -points per axis in the in-plane a - and b -directions inversely proportional to the supercell size: $4 \times 4 \times 4$, $3 \times 3 \times 4$, and $2 \times 2 \times 4$ k -points per axis were used for $2 \times 2 \times 1$, $3 \times 3 \times 1$, and $4 \times 4 \times 1$ supercells, respectively. Atomic coordinates were relaxed using force thresholds of 10^{-4} Ry/Bohr and the stresses were relaxed to 0.1 kbar. Calculations were spin-unpolarized, except for ferromagnetic bulk Ni. Spin-polarization for other cases was found to affect the total energy by less than 0.001 meV per atom, thus having no significance for the properties considered here. The change is only non-negligible in bulk Ni, where the energy difference is 0.2 eV/atom.

A wavefunction cutoff of 60 Ry was used for PBE and 80 Ry for LDA. The self-consistency thresholds were set to 10^{-18} for the ground state and 10^{-15} for phonons. Strict thresholds

were required for accurate calculations of modes with low frequencies. Low frequencies of vibrational calculations of 3×3 t-intercalation and Mo substitution were initially calculated to be imaginary and required special care to properly converge: k -points were increased to $4 \times 4 \times 4$ and the phonon self-consistent threshold was lowered to 10^{-16} . DOS calculations were carried out on fine k -grid meshes of $12 \times 12 \times 12$, $10 \times 10 \times 10$, $6 \times 6 \times 6$, and $6 \times 6 \times 6$ for $1 \times 1 \times 1$, $2 \times 2 \times 1$, $3 \times 3 \times 1$, and $4 \times 4 \times 1$ supercell sizes, respectively.

3.2 Elasticity

Elastic parameters were calculated using the stress-strain relationship (using Voigt notation) $\sigma_i = C_{ij}\epsilon_j$. We applied uniaxial strains in the 1- and 3-directions and 5-direction shear strains to calculate C_{11} , C_{33} , and C_{55} . Strains were applied from -0.01 to 0.01 in intervals of 0.002, with each structure’s atoms relaxed while holding the lattice vectors constant. C_{ij} was determined by linear regression on the stress *vs.* strain. Elastic parameters for pristine structures using different functionals are listed in Table 1, demonstrating good agreement for LDA and PBE+GD2 with experiment.

Strain directions 3 and 5 were chosen for their relevance to sliding and wear. Shearing strains in the 4- and 5-directions are the motions involved in basal plane sliding. Uniaxial 3-strain is involved in layer separation, leading to wear. By symmetry, $C_{11} = C_{22}$ and $C_{44} = C_{55}$ in pristine MoS₂, and these relations still approximately hold in our doped structures.

3.3 Formation Energy

Formation energies, E_{form} , can be used to gauge the relative stability of a structure versus a reference,^{49,87} and are defined as:

$$E_{\text{form}} = E_{\text{mixed}} - \sum_i N_i \mu_i \tag{1}$$

E_{mixed} is the energy of the material of interest, μ_i is the chemical potential of the bulk element i , and N_i is the number of atoms of element i in the mixed system. μ_i must be less than the bulk element’s energy per atom for the formation of the material of interest to be thermodynamically favored compared to its bulk elements, E_i . For this reason, it is useful to write Eqn. 1 instead using $\Delta\mu \equiv \mu_i - E_i$, so

$$E_{\text{form}} = E_{\text{mixed}} - \sum_i N_i(\Delta\mu_i + E_i) \quad (2)$$

Formation energies were all referenced against the most stable bulk elemental compounds: Fm $\bar{3}$ m (fcc) Ni, Im $\bar{3}$ m (bcc) Mo, and P2 $_1$ S. S is a particularly difficult element to handle, given its natural state is 8-membered rings. This S structure was chosen as it has been used in other literature^{62,88} and had the lowest calculated energy per atom among an isolated S atom, S $_2$ molecule, an isolated 8-membered ring, and an arrangement of 4 8-membered rings per cell. The reference elemental structures are metals in the case of Ni and Mo while the structures of interest are mostly semiconducting. This leads to the required use of smearing on the electronic states of some of the structures. Furthermore, some structures have significant Van der Waals interactions while others do not. These differences motivate LDA for direct comparison of formation energies rather than PBE or PBE + GD2. Lattice parameters, Materials Project IDs, k -grids, and space group symmetries for all of the mentioned structures can be found in Table S1. Formation energies are shown in Table S4.

Using Eqn. 2, we can compare the formation energies of doped structures to construct zones of chemical potentials that favor the formation of one structure over another at a given supercell size as in Fig. 3. To find these regions, we need to solve for when $E_{\text{form}}(\Delta\mu_{\text{Ni}}, \Delta\mu_{\text{Mo}}, \Delta\mu_{\text{S}})$ of one structure is smaller than another. Since each computation only contains one Ni atom per supercell, we can remove the dependence of $\Delta\mu_{\text{Ni}}$, leaving us with zones as a function of only $\Delta\mu_{\text{Mo}}$ and $\Delta\mu_{\text{S}}$.

We represent phase stability using the concept of the convex hull⁸⁹ which we compute

using Mathematica.⁹⁰ Considering the closed system ($\Delta\mu = 0$) at zero temperature and pressure, we can use the formation energies to construct the convex hull as the smallest convex set containing the points $(x_{\text{Ni}}, x_{\text{Mo}}, x_{\text{S}}, E_{\text{form}}/N_{\text{atoms}})$, where $x_i = N_i/(N_{\text{atoms}})$.⁸⁹ Since $\sum_i x_i = 1$, we can represent the three x_i dimensions as three legs of the two-dimensional triangle, as in Fig. 4. The $E_{\text{form}}/N_{\text{atoms}}$ axis is out of the page, but we can further simplify this representation by showing only the lines connecting points on the convex hull. Stable structures will be on the convex hull’s boundary. Any structure whose computed energy is above the convex hull is favored to phase-segregate to the structures at the nearest nodes. The energies above hull are listed in Table 2 for LDA and PBE+GD2 in Table S3. One-dimensional convex hull diagrams with reference structures that are not bulk elemental phases are shown in Fig. S2.

Supporting Information Available

Phase diagrams and convex hull diagrams for LDA, PBE, and PBE+GD2; convex hull diagrams with non-elemental references; formation energies with respect to bulk elemental structures and filling pre-existing vacancies; Materials Project ID, k -grid, and cell parameters for the structures besides Ni-doped MoS₂ featured in this work; and vibrational density of states and vibrational mode characterizations (PDF). XSF file format structures of Ni-doped MoS₂ structures relaxed with PBE+GD2 (ZIP). AXSF file format structures of Ni-doped MoS₂ vibrational eigenmodes, calculated with LDA (ZIP).

Acknowledgement

We acknowledge useful discussions with Mehmet Z. Baykara and Ashlie Martini. We acknowledge support from UC Merced start-up funds and from the Merced nAnomaterials Center for Energy and Sensing (MACES), a NASA-funded research and education center, under award NNX15AQ01. This work used computational resources from the Multi-

Environment Computer for Exploration and Discovery (MERCED) cluster at UC Merced, funded by National Science Foundation Grant No. ACI-1429783, and the National Energy Research Scientific Computing Center (NERSC), a U.S. Department of Energy Office of Science User Facility operated under Contract No. DE-AC02-05CH11231.

References

- (1) Bernardi, M.; Ataca, C.; Palumbo, M.; Grossman, J. C. Optical and Electronic Properties of Two-Dimensional Layered Materials. *Nanophotonics* **2017**, *6*, 479–493.
- (2) Molina-Sánchez, A.; Hummer, K.; Wirtz, L. Vibrational and Optical Properties of MoS₂: From Monolayer to Bulk. *Surf. Sci. Rep.* **2015**, *70*, 554–586.
- (3) Sanikop, R.; Sudakar, C. Tailoring Magnetically Active Defect Sites in MoS₂ Nanosheets for Spintronics Applications. *ACS Appl. Nano Mater.* **2020**, *3*, 576–587.
- (4) Latzke, D. W.; Zhang, W.; Suslu, A.; Chang, T.-R.; Lin, H.; Jeng, H.-T.; Tongay, S.; Wu, J.; Bansil, A.; Lanzara, A. Electronic Structure, Spin-Orbit Coupling, and Inter-layer Interaction in Bulk MoS₂ and WS₂. *Phys. Rev. B* **2015**, *91*, 235202.
- (5) Vazirisereshk, M. R.; Martini, A.; Strubbe, D. A.; Baykara, M. Z. Solid Lubrication with MoS₂: A Review. *Lubricants* **2019**, *7*, 57.
- (6) Mao, J.; Wang, Y.; Zheng, Z.; Deng, D. The Rise of Two-Dimensional MoS₂ for Catalysis. *Front. Phys.* **2018**, *13*, 138118.
- (7) Wang, D.; Zhang, X.; Shen, Y.; Wu, Z. Ni-Doped MoS₂ Nanoparticles as Highly Active Hydrogen Evolution Electrocatalysts. *RSC Adv.* **2016**, *6*, 16656–16661.
- (8) Mosconi, D.; Till, P.; Calvillo, L.; Kosmala, T.; Garoli, D.; Debellis, D.; Martucci, A.; Agnoli, S.; Granozzi, G. Effect of Ni Doping on the MoS₂ Structure and Its Hydrogen Evolution Activity in Acid and Alkaline Electrolytes. *Surfaces* **2019**, *2*, 531–545.

- (9) Stupp, B. C. Synergistic Effects of Metals Co-Sputtered with MoS₂. *Thin Solid Films* **1981**, *84*, 257–266.
- (10) Vellore, A.; Garcia, S. R.; Walters, N.; Johnson, D. A.; Kennett, A.; Heverly, M.; Martini, A. Ni-Doped MoS₂ Dry Film Lubricant Life. *Adv. Mater. Interfaces* **2020**, 2001109.
- (11) Tedstone, A. A.; Lewis, D. J.; O'Brien, P. Synthesis, Properties, and Applications of Transition Metal-Doped Layered Transition Metal Dichalcogenides. *Chem. Mater.* **2016**, *28*, 1965–1974.
- (12) Sun, M.; Nelson, A. E.; Adjaye, J. On the Incorporation of Nickel and Cobalt into MoS₂-Edge Structures. *J. Catal.* **2004**, *226*, 32–40.
- (13) Rangarajan, S.; Mavrikakis, M. Adsorption of Nitrogen- and Sulfur-Containing Compounds for NiMoS for Hydrotreating Reactions: A DFT and vdW-Corrected Study. *AIChE J* **2015**, *61*, 4036–4050.
- (14) Lauritsen, J. V.; Kibsgaard, J.; Olesen, G. H.; Moses, P. G.; Hinnemann, B.; Helveg, S.; Nørskov, J. K.; Clausen, B. S.; Topsøe, H.; Lægsgaard, E.; Besenbacher, F. Location and Coordination of Promoter Atoms in Co- and Ni-Promoted MoS₂-Based Hydrotreating Catalysis. *J. Catal.* **2007**, *249*, 220–233.
- (15) Wambeke, A.; Jalowiecki, L.; Kasztelan, S.; J., G.; Bonnelle, J. P. The Active Site for Isoprene Hydrogenation on MoS₂/γ-Al₂O₃ Catalysts. *J. Catal.* **1988**, *109*, 320–328.
- (16) Hakala, M.; Kronberg, R.; Laasonen, K. Hydrogen Adsorption on Doped MoS₂ Nanostructures. *Sci. Rep.* **2017**, *7*, 15243.
- (17) Kondekar, N.; Boebinger, M. G.; Tian, M.; Kirmani, M. H.; McDowell, M. T. The Effect of Nickel on MoS₂ Growth Revealed with *in Situ* Transmission Electron Microscopy. *ACS Nano* **2019**, *13*, 7117–7126.

- (18) Attanayake, N. H.; Thenuwara, A. C.; Patra, A.; Aulin, Y. V.; Tran, T. M.; Chakraborty, H.; Borguet, E.; Klein, M. L.; Perdew, J. P.; Strongin, D. R. Effect of Intercalated Metals and the Electrocatalytic Activity of 1T-MoS₂ for the Hydrogen Evolution Reaction. *ACS Energy Lett.* **2018**, *3*, 7–13.
- (19) Tsai, M.-L.; Su, S.-H.; Chang, J.-K.; Tsai, D.-S.; Chang-Hsiao, C.; Wu, C.-I.; Li, L.-J.; Chen, L.-J.; He, J.-H. Monolayer MoS₂ Heterojunction Solar Cells. *ACS Nano* **2014**, *8*, 8317–8322.
- (20) Li, P.; Yuan, K.; Lin, D.-Y.; Xu, X.; Wang, Y.; Wan, Y.; Yu, H.; Zhang, K.; Ye, Y.; Dai, L. A Mixed-Dimensional Light-Emitting Diode Based on a p-MoS₂ Nanosheet and an n-CdSe Nanowire. *Nanoscale* **2017**, *46*, 18175–18179.
- (21) Bernardi, M.; Palummo, M.; Grossman, J. C. Extraordinary Sunlight Absorption and One Nanometer Thick Photovoltaics Using Two-Dimensional Monolayer Materials. *Nano Lett.* **2013**, *13*, 3664–3670.
- (22) Zhong, M.; Shen, C.; Huang, L.; Deng, H.-X.; Shen, G.; Zheng, H.; Wei, Z.; Li, J. Electronic Structure and Exciton Shifts in Sb-Doped MoS₂ Monolayer. *npj 2D Mater. Appl.* **2019**, *3*, 1.
- (23) Schaibley, J. R.; Yu, H.; Clark, G.; Rivera, P.; Ross, J. S.; Seyler, K. L.; Yao, W.; Xu, X. Valleytronics in 2D Materials. *Nat. Rev. Mater.* **2016**, *1*, 16055.
- (24) Cheng, Y. C.; Zhu, Z. Y.; Mi, W. B.; Guo, Z. B.; Schwingenschlögl, U. Prediction of Two-Dimensional Diluted Magnetic Semiconductors: Doped Monolayer MoS₂ Systems. *Phys. Rev. B* **2013**, *87*, 100401(R).
- (25) Martin, J.-M. In *Superlubricity*; Erdemir, A., Martin, J.-M., Eds.; Elsevier Science B.V., 2007; pp 207–225.

- (26) Rapoport, L.; Moshkovich, A.; Perfilyev, V.; Laikhtman, A.; Lapsker, I.; Yadgarov, L.; Rosentsveig, R.; Tenne, R. High Lubricity of Re-Doped Fullerene-Like MoS₂ Nanoparticles. *Tribol. Lett.* **2012**, *45*, 257–264.
- (27) Ding, X.-Z.; Zeng, X. T.; He, X. Y.; Chen, Z. Tribological Properties of Cr- and Ti-Doped MoS₂ Composite Coatings Under Different Humidity Atmosphere. *Surf. Coat. Tech.* **2010**, *205*, 224–231.
- (28) Hu, R.; Krylov, S. Y.; Frenken, J. W. M. On the Origin of Frictional Energy Dissipation. *Tribol. Lett.* **2020**, *68*, 8.
- (29) Filleter, T.; McChesney, J. L.; Bostwick, A.; Rotenberg, E.; Emtsev, K. V.; Seyller, T.; Horn, K.; Bennewitz, R. Friction and Dissipation in Epitaxial Graphene Films. *Phys. Rev. Lett.* **2009**, *102*, 086102.
- (30) Park, S.; Park, J.; Abroshan, H.; Zhang, L.; Kim, J. K.; Zhang, J.; Guo, J.; Siahrostami, S.; Zheng, X. Enhancing Catalytic Activity of MoS₂ Basal Plane S-Vacancy by Co Cluster Addition. *ACS Energy Lett.* **2018**, *3*, 2685–2693.
- (31) Zhu, J.; Zhang, H.; Tong, Y.; Zhao, L.; Zhang, Y.; Qiu, Y.; Lin, X. First-Principles Investigations of Metal (V, Nb, Ta)-Doped Monolayer MoS₂: Structural Stability, Electronic Properties and Adsorption of Gas Molecules. *Appl. Surf. Sci.* **2017**, *419*, 522–530.
- (32) Julien, C.; Sekine, T.; Balkanski, M. Lattice Dynamics of Lithium Intercalated MoS₂. *Solid State Ion.* **1991**, *48*, 225–229.
- (33) Zou, J.; Li, F.; Bissett, M. A.; Kim, F.; Hardwick, L. J. Intercalation Behaviour of Li and Na into 3-layer and Multilayer MoS₂ Flakes. *Electrochim. Acta* **2020**, *331*, 135284.
- (34) Zhang, R.; Tsai, I.-L.; Chapman, J.; Khestanova, E.; Waters, J.; Grigorieva, I. V. Superconductivity in Potassium-Doped Metallic Polymorphs of MoS₂. *Nano Lett.* **2016**, *16*, 629–636.

- (35) Chen, M. F.; Douglass, D. L. Effect of Some Ternary Additions on the Sulfidation of Ni-Mo Alloys. *Oxid. Met.* **1990**, *33*, 103–133.
- (36) Chakraborty, B.; Bera, A.; Muthu, D. V. S.; Bhowmick, S.; Waghmare, U. V.; Sood, A. K. Symmetry-Dependent Phonon Renormalization in Monolayer MoS₂ Transistor. *Phys. Rev. B* **2012**, *85*, 161403(R).
- (37) Suh, J.; Park, T.-E.; Lin, D.-Y.; Fu, D.; Park, J.; Jung, H. J.; Chen, Y.; Ko, C.; Jang, C.; Sun, Y.; Sinclair, R.; Chang, J.; Tongay, S.; Wu, J. Doping Against the Native Propensity of MoS₂: Degenerate Hole Doping by Cation Substitution. *Nano Lett.* **2014**, *14*, 6976–6982.
- (38) Shi, Y.; Huang, J.-K.; Jin, L.; Hsu, Y.-T.; Yu, S. F.; Li, L.-J.; Yang, H. Y. Selective Decoration of Au Nanoparticles on Monolayer MoS₂ Single Crystals. *Sci. Rep.* **2013**, *3*, 1839.
- (39) Tangney, P.; Cohen, M. L.; Louie, S. G. Giant Wave-Drag Enhancement of Friction in Sliding Carbon Nanotubes. *Phys. Rev. Lett.* **2006**, *97*, 195901.
- (40) Wilson, J. A.; Yoffe, A. D. The Transition Metal Dichalcogenides: Discussion and Interpretation of the Observed Optical, Electrical and Structural Properties. *Adv. Phys.* **1969**, *18*, 193–335.
- (41) Molina-Sánchez, A.; Wirtz, L. Phonons in Single-Layer and Few-Layer MoS₂ and WS₂. *Phys. Rev. B* **2011**, *84*, 155413.
- (42) Yengejeh, S. I.; Junxian, L.; Kazemi, S. A.; Wen, W.; Wang, Y. Effect of Structural Phases on Mechanical Properties of Molybdenum Disulfide. *ACS Omega* **2020**, *5*, 5994–6002.
- (43) Livneh, T.; Spanier, J. E. A Comprehensive Multiphonon Spectral Analysis in MoS₂. *2D Mater.* **2015**, *2*, 035003.

- (44) Coutinho, S. S.; Tavares, M. S.; Barboza, C. A.; Frazão, N.; Moreira, E.; Azevedo, D. L. 3R and 2H Polytypes of MoS₂: DFT and DFPT Calculations of Structural, Optoelectronic, Vibrational and Thermodynamic Properties. *J. Phys. Chem. Solids* **2017**, *111*, 25–33.
- (45) Feldman, J. L. Elastic Constants of 2H-MoS₂ and 2H-NbSe₂ Extracted from Measured Dispersion Curves and Linear Compressibilities. *J. Phys. Chem. Solids* **1976**, *37*, 1141–1144.
- (46) Todorova, T.; Alexiev, V.; Prins, R.; Weber, T. *Ab Initio* Study of 2H-MoS₂ using Hay and Wadt Effective Core Pseudo-Potentials for Modelling the (10 $\bar{1}$ 0) Surface Structure. *Phys. Chem. Chem. Phys.* **2004**, *6*, 3023–3030.
- (47) Tkatchenko, A.; Scheffler, M. Accurate Molecular Van Der Waals Interactions from Ground-State Electron Density and Free-Atom Reference Data. *Phys. Rev. Lett.* **2009**, *102*, 073005.
- (48) Grimme, S.; Antony, J.; Ehrlich, S.; Krieg, H. A Consistent and Accurate *Ab Initio* Parametrization of Density Functional Dispersion Correction (DFT-D) for the 94 Elements H-Pu. *J. Chem. Phys.* **2010**, *132*, 154104.
- (49) Ivanovskaya, V. V.; Zobelli, A.; Gloter, A.; Brun, N.; Serin, V.; Colliex, C. *Ab Initio* Study of Bilateral Doping within the MoS₂-NbS₂ System. *Phys. Rev. B* **2008**, *78*, 134104.
- (50) Chen, X.; Chen, Z.; Jun, L. Critical Electronic Structures Controlling Phase Transitions Induced by Lithium Ion Intercalation in Molybdenum Disulphide. *Chin. Sci. Bull.* **2013**, *58*, 1632–1641.
- (51) Grimme, S. Semiempirical GGA-type Density Functional Constructed with a Long-Range Dispersion Correction. *J. Comput. Chem.* **2006**, *27*, 1787–1799.

- (52) Andersson, M. P. Density Functional Theory with Modified Dispersion Correction for Metals Applied to Self-Assembled Monolayers of Thiols on Au(111). *J. Theor. Chem.* **2013**, *2013*, 327839.
- (53) Yin, M. T.; Cohen, M. L. Structural Theory of Graphite and Graphitic Silicon. *Phys. Rev. B* **1984**, *29*, 6996–6998.
- (54) Peelaers, H.; Van de Walle, C. G. Elastic Constants and Pressure-Induced Effects in MoS₂. *J. Phys. Chem. C* **2014**, *118*, 12073–12076.
- (55) Peelaers, H.; Van de Walle, C. G. First-Principles Study of Van der Waals Interactions in MoS₂ and MoO₃. *J. Phys.: Condens. Matter* **2014**, *26*, 305502.
- (56) Jain, A.; Ong, S. P.; Hautier, G.; Chen, W.; Richards, W. D.; Dacek, S.; Cholia, S.; Gunter, D.; Skinner, D.; Ceder, G.; Persson, K. A. Commentary: The Materials Project: A Materials Genome Approach to Accelerating Materials Innovation. *APL Materials* **2013**, *1*, 011002.
- (57) Guillevic, J.; Bars, M. O.; Grandjean, D. Etude Structurale de Combinaisons Sulfurées et Sélieniées du Molybdène: III. Structure Cristalline de NiMo₃S₄. *J. Solid State Chem.* **1973**, *7*, 158–162.
- (58) Enyashin, A. N.; Seifert, G. Density-Functional Study of Li_xMoS₂ Intercalates ($0 \leq x \leq 1$). *Comput. Theor. Chem.* **2012**, *999*, 13–20.
- (59) Kokalj, A. XCrySDen—A New Program for Displaying Crystalline Structures and Electron Densities. *J. Mol. Graph. Model.* **1999**, *17*, 176–179.
- (60) Zhang, S. B.; Wei, S.-H.; Zunger, A.; Katayama-Yoshida, H. Defect Physics of the CuInSe₂ Chalcopyrite Semiconductor. *Phys. Rev. B* **1998**, *57*, 9642–9656.
- (61) Zhao, X. et al. Engineering Covalently Bonded 2D Layered Materials by Self-Intercalation. *Nature* **2020**, *581*, 171–177.

- (62) Dolui, K.; Rungger, I.; Pemmaraju, C. D.; Sanvito, S. Possible Doping Strategies for MoS₂ Monolayers: An *Ab Initio* Study. *Phys. Rev. B* **2013**, *88*, 075420.
- (63) Jain, A.; Hautier, G.; Ong, S. P.; Moore, J., Charles; Fischer, C. C.; Persson, K. A.; Ceder, G. Formation Enthalpies by Mixing GGA and GGA + *U* Calculations. *Phys. Rev. B* **2011**, *84*, 045115.
- (64) Kutana, A.; Penev, E. S.; Yakobson, B. I. Engineering Electronic Properties of Layered Transition-Metal Dichalcogenide Compounds through Alloying. *Nanoscale* **2014**, *6*, 5820.
- (65) Mignuzzi, S.; Pollard, A. J.; Bonini, N.; Brennan, B.; Gilmore, I. S.; Pimenta, M. A.; Richards, D.; Roy, D. Effects of Disorder on Raman Scattering of Single-Layer MoS₂. *Phys. Rev. B* **2015**, *91*, 195411.
- (66) Iqbal, M. W.; Shahzad, K.; Akbar, R.; Hussain, G. A Review on Raman Finger Prints of Doping and Strain Effect in TMDCs. *Microelectron. Eng.* **2020**, *219*, 111152.
- (67) Yuan, H.; Zhou, X.; Cao, Y.; Bian, Q.; Zhang, Z.; Sun, H.; Li, S.; Shao, Z.; Hu, J.; Zhu, Y.; Mao, Z.; Ji, W.; Pan, M. Raman Detection of Hidden Phonons Assisted by Atomic Point Defects in a Two-Dimensional Semimetal. *npj 2D Mater. Appl.* **2019**, *3*, 12.
- (68) Zhang, F.; Lu, Y.; Schulman, D. S.; Zhang, T.; Fujisawa, K.; Lin, Z.; Lei, Y.; Elias, A. L.; Das, S.; Sinnott, S. B.; Terrones, M. Carbon Doping of WS₂ Monolayers: Bandgap Reduction and *p*-Type Doping Transport. *Sci. Adv.* **2019**, *5*, 5.
- (69) Sekine, T.; C., J.; Samaras, I.; Jouanne, M.; Balkanski, M. Vibrational Modifications on Lithium Intercalation in MoS₂. *Mat. Sci. Eng. B* **1989**, *3*, 153–158.
- (70) Vandalon, V.; Verheijen, M. A.; Kessels, W. M. M.; Bol, A. A. Atomic Layer Deposition

- of Al-Doped MoS₂: Synthesizing a *p*-type 2D Semiconductor with Tunable Carrier Density. *ACS Appl. Nano Mater.* **2020**, *3*, 10200–10208.
- (71) Kim, J.; Lee, J.-U.; Cheong, H. Polarized Raman Spectroscopy for Studying Two-Dimensional Materials. *J. Phys.: Condens. Matter* **2020**, *32*, 343001.
- (72) Lin, M.-L.; Zhou, Y.; Wu, J.-B.; Cong, X.; Liu, X.-L.; Zhang, J.; Li, H.; Yao, W.; Tan, P.-H. Cross-Dimensional Electron-Phonon Coupling in Van der Waals Heterostructures. *Nat. Commun.* **2019**, *10*, 2419.
- (73) Komsa, H.-P.; Krasheninnikov, A. V. Native Defects in Bulk and Monolayer MoS₂ from First Principles. *Phys. Rev. B* **2015**, *91*, 125304.
- (74) Gómez-Balderas, R.; Martínez-Magadán, J. M.; Santamaria, R.; Amador, C. Promotional Effect of Co or Ni Impurity in the Catalytic Activity of MoS₂: An Electronic Structure Study. *Int. J. Quantum Chem.* **2000**, *80*, 406–415.
- (75) Ostadhossein, A.; Rahnamoun, A.; Wang, Y.; Zhao, P.; Zhang, S.; Crespi, V. H.; van Duin, A. C. T. ReaxFF Reactive Force-Field Study of Molybdenum Disulfide (MoS₂). *J. Phys. Chem. Lett.* **2017**, *8*, 631–640.
- (76) Liang, T.; Sawyer, W. G.; Perry, S. S.; Sinnott, S. B.; Phillpot, S. R. First-Principles Determination of Static Potential Energy Surfaces for Atomic Friction in MoS₂ and MoO₃. *Phys. Rev. B* **2008**, *77*, 104105.
- (77) Karkee, R.; Guerrero, E.; Strubbe, D. A. Structure and Energetics of Ni-doped MoS₂ Monolayers and Polytypes from Density Functional Theory. *arXiv:2008.04301* **2020**,
- (78) Baroni, S.; de Gironcoli, S.; Dal Corso, A. Phonons and Related Crystal Properties from Density-Functional Perturbation Theory. *Rev. Mod. Phys.* **2001**, *73*, 515–562.
- (79) Giannozzi, P. et al. Advanced Capabilities for Materials Modelling with QUANTUM ESPRESSO. *J. Phys.: Condens. Matter* **2017**, *29*, 465901.

- (80) Giannozzi, P. et al. **QUANTUM ESPRESSO**: a Modular and Open-Source Software Project for Quantum Simulations of Materials. *J. Phys.: Condens. Matter* **2009**, *21*, 395502.
- (81) Perdew, J. P.; Burke, K.; Ernzerhof, M. Generalized Gradient Approximation Made Simple. *Phys. Rev. Lett.* **1996**, *77*, 3865–3868.
- (82) Perdew, J. P.; Wang, Y. Accurate and Simple Analytic Representation of the Electron-gas Correlation Energy. *Phys. Rev. B* **1992**, *45*, 13244.
- (83) Hamann, D. R. Optimized Norm-Conserving Vanderbilt Pseudopotentials. *Phys. Rev. B* **2013**, *88*, 085117.
- (84) Schlipf, M.; Gygi, F. Optimization Algorithm for the Generation of ONCV Pseudopotentials. *Comput. Phys. Commun.* **2015**, *196*, 36–44, http://www.quantum-simulation.org/potentials/sg15_oncv/.
- (85) van Setten, M. J.; Giantomassi, M.; Bousquet, E.; Verstraete, M. J.; Hamann, D. R.; Gonze, X.; Rignanese, G.-M. The PseudoDojo: Training and Grading a 85 Element Optimized Norm-Conserving Pseudopotential Table. *Comput. Phys. Commun.* **2018**, *226*, 39–54, <http://www.pseudo-dojjo.org/>.
- (86) Lazzeri, M.; Mauri, F. First-Principles Calculation of Vibrational Raman Spectra in Large Systems: Signature of Small Rings in Crystalline SiO₂. *Phys. Rev. Lett.* **2003**, *90*.
- (87) Kim, N.; Martin, P. P.; Rockett, A. A.; Ertekin, E. Screened-Exchange Density Functional Theory Description of the Electronic Structure and Phase Stability of the Chalcopyrite Materials AgInSe₂ and AuInSe₂. *Phys. Rev. B* **2016**, *93*, 165202.
- (88) Rasmussen, F. A.; Thygesen, K. S. Computational 2D Materials Database: Electronic Structure of Transition-Metal Dichalcogenides and Oxides. *J. Phys. Chem. C* **2015**, *119*, 13169–13183.

- (89) Ong, S. P.; Wang, L.; Kang, B.; Ceder, G. Li—Fe—P—O₂ Phase Diagram from First Principles Calculations. *Chem. Mater.* **2008**, *20*, 1798–1807.
- (90) Wolfram Research Inc., Mathematica 12.1. 2020.

TOC Graphic

